SIAM J. Applied Dynamical Systems
Vol. 18, No. 2, pp. 1060–1077

Effects of Periodic Forcing on a Paleoclimate Delay Model*

Courtney Quinn†, Jan Sieber‡, and Anna S. von der Heydt§

Abstract. We present a study of a delay differential equation (DDE) model for the Mid-Pleistocene Transition (MPT). We investigate the behavior of the model when subjected to periodic forcing. The unforced model has a bistable region consisting of a stable equilibrium along with a large-amplitude stable periodic orbit. We study how forcing affects solutions in this region. Forcing based on astronomical data causes a sudden transition in time and under increase of the forcing amplitude, moving the model response from a non-MPT regime to an MPT regime. Similar transition behavior is found for periodic forcing. A bifurcation analysis shows that the transition is due not to a bifurcation but instead to a shifting basin of attraction. While determining the basin boundary we demonstrate how one can accurately compute the intersection of a stable manifold of a saddle with a slow manifold in a DDE by embedding the algorithm for planar maps proposed by England, Krauskopf, and Osinga [*SIAM J. Appl. Dyn. Syst.*, 3 (2004), pp. 161–190] into the equation-free framework by Kevrekidis and Samaey [*Rev. Phys. Chem.*, 60 (2009), pp. 321–344].

Key words. delay, paleoclimate, bifurcation, Mid-Pleistocene Transition, equation-free methods, dimension reduction

AMS subject classifications. 37M20, 86A04, 37C55, 37B55, 34K28

DOI. 10.1137/18M1203079

1. Introduction.

Low-dimensional conceptual models are often used in climate modeling to understand basic interactions between specific climate variables [10]. These are particularly useful when studying long time-scale dynamics and computing power precludes resolving all of the many temporal and spatial scales [20]. For this reason, conceptual models are essential in studying past climates of the earth and their long-term variability.

The Pleistocene, which lasted from approximately 2.6 Myr to 11.7 kyr before present (BP), is a period in climate history that particularly benefits from this type of modeling. The essential variability can be captured through dynamical systems with only a few coupled variables

*Received by the editors July 26, 2018; accepted for publication (in revised form) March 21, 2019; published electronically June 4, 2019.
http://www.siam.org/journals/siads/18-2/M120307.html
Funding: The work of the first and second authors was supported in part by the European Union's Horizon 2020 research and innovation program under the Marie Sklodowska-Curie grant agreement 643073. The work of the second author was also supported in part by EPSRC via grants EP/N023544/1 and EP/N014391/1. The work of the third author was supported by the EPSRC funded Past Earth Network (grant EP/M008363/1) and ReCoVER (grant EP/M008495/1) for an extended research visit to the University of Exeter in Summer 2017.
†College of Engineering, Mathematics, and Physical Sciences, University of Exeter, Exeter EX4 4QE, United Kingdom. Current address: CSIRO Oceans and Atmosphere, Decadal Climate Forecasting Project, Hobart, Tasmania 7000, Australia (courtney.quinn@csiro.au).
‡College of Engineering, Mathematics, and Physical Sciences, University of Exeter, Exeter EX4 4QE, United Kingdom (J.Sieber@exeter.ac.uk).
§Institute for Marine and Atmospheric Research, Department of Physics & Center for Complex Systems Studies, Utrecht University, Princetonplein 5, 3584 CC Utrecht, The Netherlands (A.S.vonderHeydt@uu.nl).

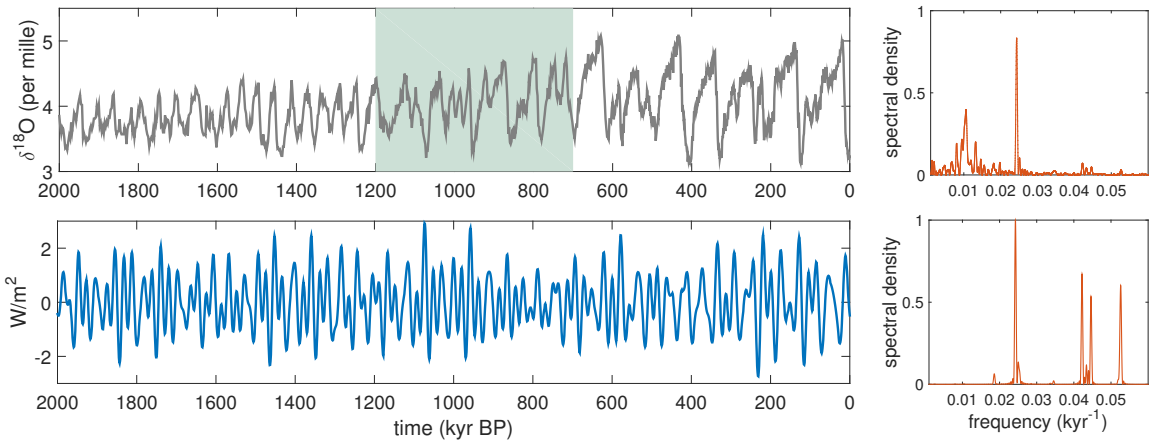

Figure 1. *(Top) Proxy record of global ice cover for the last* 2 *Myr* [23] *and its spectrum. (Bottom) Normalized integrated July insolation* $F_I(t)$ *at* $65°N$*, adapted from* [18]*, and its spectrum.*

(see the review [8] for an extensive collection of examples). During this time, the earth experienced many oscillations between periods of colder temperatures and increased global ice cover (*glacials*) and periods of warmer temperatures with less global ice cover (*interglacials*) [19]. The dominant periodicity of the oscillations also changed from approximately 41 kyr in the beginning of the Pleistocene to roughly 100 kyr towards the end of the Pleistocene, together with an increase in amplitude and degree of asymmetry in the oscillations [16, 24]. This shift in dynamics is known as the Mid-Pleistocene Transition (MPT), and the exact timing of it is believed to be sometime between 1200 and 700 kyr BP [24, 31, 8, 10, 13]. The oscillations and the MPT can be observed through proxy records as shown in Figure 1.

In a recent study [32] we revisited a model of the Pleistocene introduced by Saltzman and Maasch [34]. This model was used to replicate the main dynamics of the ice ages, which involved perturbations in global ice mass, atmospheric CO_2, and global ocean circulation. In the original study, the authors of [34] showed that this particular model was able to reproduce the MPT through a slow parameter shift. In our study [32] we reduced this model to a scalar delay differential equation (DDE) for global ice mass. Through analytical and numerical investigations we showed that the models were qualitatively equivalent. Our main focus of the study was on the bistable region found in both the original ODE model and the DDE model, a region which was not explored in the original analyses [34, 25]. We observed the behavior within this region when the model was subjected to external forcing, namely, solar radiation, and were able to reproduce an MPT-like transition without any change in parameters.

Very early studies have shown a relationship between solar radiation and the glacial cycles [29, 6, 36]. The solar radiation, otherwise known as astronomical insolation, is a quasiperiodic forcing with dominant frequencies around 0.0243, 0.0434, and 0.0526 kyr^{-1}, corresponding to periodicities of 41, 23, and 19 kyr, respectively (see Figure 1) [4, 17]. The most prominent signal in the forcing is at 41 kyr, and this has been argued to be the driving force of the climate fluctuations in the beginning of the Pleistocene [29], while it still remains unclear where the longer-term and large-amplitude fluctuations of the late Pleistocene derive from and why a

transition from the 41 kyr to the 100 kyr dominant periodicity occurred [30]. It is natural then to consider the effects of the 41 kyr signal alone on our model. In this paper we perform a systematic study of how the model responds to periodic forcing with a period of 41 kyr.

The paper is organized as follows. We summarize the numerical observations and the bifurcation analysis of the unforced system from our recent study [32] in section 2. Section 3 studies the effects of periodic forcing, showing that one type of transition observed in [32] can be attributed to a shift in basin boundaries in the context of periodic forcing. We are able to track the precise basin boundary by applying algorithms developed for stable manifolds of two-dimensional maps to the forced DDE. Section 4 compares our results to other hypotheses, also suggesting how the theory for quasiperiodically forced systems could be applied to extend our results.

2. Background.

Our delay equation model of global ice mass perturbations as described in [32] is as follows:

$$\dot{X}(t) = -pX(t-\tau) + rX(t) - sX(t-\tau)^2 - X(t-\tau)^2 X(t). \tag{1}$$

Here, X represents the ice mass anomaly from a background state where $X(t)$ and $X(t-\tau)$ are taken at present and τ years in the past, respectively. The delay τ is the time scale of the feedback processes associated with ice accumulation and decay, and with carbon storage and transport in the deep ocean. This is the parameter we are most interested in analyzing. The other parameters, p, r, and s, will be kept constant at $p = 0.95$, $r = 0.8$, and $s = 0.8$ in accordance with [34] for all numerical studies. The unit for time t and delay τ is 10 kyr throughout the paper, unless the time unit is explicitly specified (then the time axis is usually kyr BP, as in Figure 1).

This is not the first time a delay model has been suggested for the dynamics of the Pleistocene. Bhattacharya, Ghil, and Vulis [5] explored an energy balance model which incorporates a delay related to feedback effects from the reflectivity of the earth's surface. Additionally, Ghil, Mullhaupt, and Pestiaux [15] proposed a Boolean delay model for global temperature, northern hemisphere ice volume, and deep-ocean circulation, with delays corresponding to ice sheet expansion, ice accumulation, and overturning time of the deep ocean. The three delay effects discussed in [15] are captured within our delayed feedback model.

2.1. Internal dynamics.

We conducted a bifurcation analysis of the model for realistic values of the delay, $\tau \in (1, 2)$. There were five distinct regions with respect to global stability (see Figure 2). They are as follows:

- $[r_{\mathrm{ee}}]$ two stable equilibria,
- $[r_{\mathrm{es}}]$ one stable equilibrium and one stable small-amplitude periodic orbit,
- $[r_{\mathrm{e}}]$ one stable equilibrium,
- $[r_{\mathrm{el}}]$ one stable equilibrium and one stable large-amplitude periodic orbit, and
- $[r_{\mathrm{l}}]$ one stable large-amplitude periodic orbit.

The bistable region, r_{el}, for $\tau \in [1.295, 1.625]$ with a stable equilibrium and a large-amplitude stable periodic orbit was not previously explored. Within this region, if the model is subjected to external forcing, transitions are possible between the two stable states without any change in parameters.

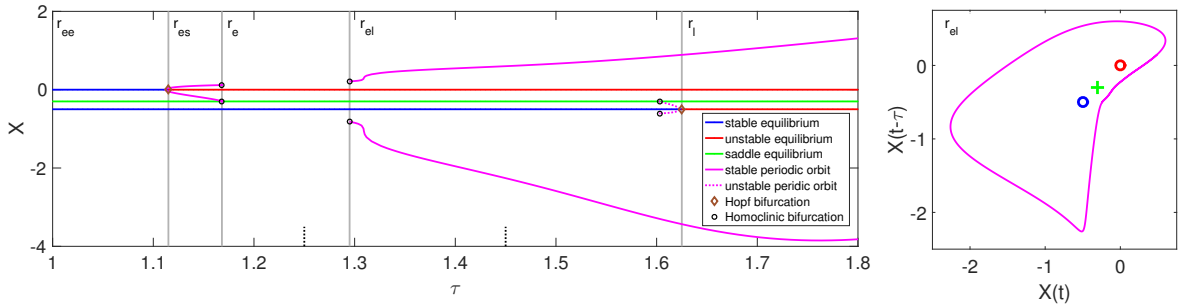

Figure 2. *(Left) Bifurcation diagram of the DDE model* (1) *for delay parameter* τ. *The dotted black lines indicate values of* τ *used in forcing studies:* $\tau_{\text{ref}} = 1.25$ *and* $\tau_{\text{bist}} = 1.45$. *Figure adapted from* [32]. *(Right) Phase portrait of the bistable region* r_{el}, $\tau_{\text{bist}} = 1.45$. *The circles are the stable (blue) and unstable (red) equilibria, the green cross is the saddle equilibrium, and the pink curve shows the periodic orbit. Other parameters:* $p = 0.95$, $r = s = 0.8$.

We also make a note about the dimensionality of the system. Although DDEs are infinite-dimensional, the phase portrait in Figure 2 gives initial evidence that the dynamics are confined to a two-dimensional slow manifold. Engler et al. [13] derived a two-dimensional slow manifold for the original model [34] through considering the deep ocean time scale as instantaneous ($\tau = 1$). Here we consider the case where the deep ocean time scale is not instantaneous ($\tau > 1$). The dimensionality will be investigated in more detail in subsection 3.2.

2.2. Astronomical forcing leading to sudden transition. Quinn et al. [32] studied the model's response in the bistable region r_{el} when subjected to astronomical forcing using simulations. They included the forcing as an additive term (with negative amplitude as insolation reduces ice mass),

$$\dot{X}(t) = -pX(t-\tau) + rX(t) - sX(t-\tau)^2 - X(t-\tau)^2 X(t) - uF_I(t). \tag{2}$$

The term $F_I(t)$ is the forcing signal, shown in Figure 1, which is a time series of integrated summer insolation at 65°N computed by Huybers and Eisenman [18] based on the model in [17]. Details of how the forcing curve in Figure 1 was obtained from publicly available data are given in [32]. The data was obtained through numerical approximation of changes in the long-term planetary motion based on the theory for long-term variation of daily insolation by Berger [4]. As discussed by Huybers [17], the forcing is dominated by a quasiperiodic superposition of approximately periodic variations of precession, obliquity, and eccentricity. This signal, shown in Figure 1 (bottom panel), can be approximated by a quasiperiodic function of 35 frequencies [8], with dominant frequencies corresponding to periods of around 41, 23, and 19 kyr (compare to the lower right panel of Figure 1). The parameter u represents the forcing amplitude of which the realistic value is uncertain.

Figure 3 summarizes the most important observation of Quinn et al. [32], which motivates our investigation in the following sections. For values of τ in the bistable region r_{el}, there are two possible responses for sufficiently small u, both illustrated in Figure 3(a): a *small-amplitude* (green in Figure 3(a)) and a *large-amplitude* (purple) response. Each response is a perturbation of an attractor of the unforced system, namely, the equilibrium and the large-amplitude periodic orbit, which persist for small u. The green time profile has been computed

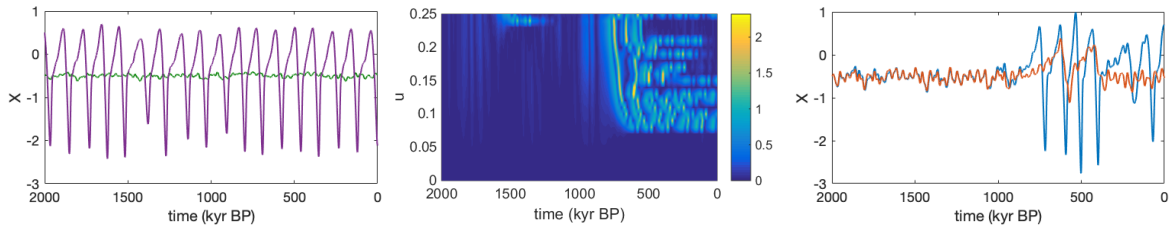

(a) (b) (c)

Figure 3. *(adapted from* [32]*)* Small-amplitude *and* large-amplitude *responses in bistable region* r_{el} *when subjected to astronomical forcing.* (a) *Example trajectories of small-amplitude (green) and large-amplitude (purple) responses for* $\tau = \tau_{\mathrm{bist}}$ *and* $u = 0.05$. (b) *Distance between trajectory for delay* $\tau_{\mathrm{bist}} = 1.45$ *and reference trajectory* $\tau_{\mathrm{ref}} = 1.25$ *at given forcing amplitude* $u \in [0, 0.25]$. *Averages taken over window length of size* τ_{bist}. (c) *Example of transitioning trajectory in bistable region for* $\tau_{\mathrm{bist}} = 1.45$ *and* $u = 0.15$ *(blue) and its reference trajectory at* $\tau_{\mathrm{ref}} = 1.25$ *and* $u = 0.15$ *(red). Initial histories* $X(s) = -0.5$ *for* $s \in [2000 + 10\tau, 2000]$ *kyr BP for panels* (b), (c) *and green response in panel* (a), $X(s) = +0.5$ *for purple response in* (a)*; parameters* $p = 0.95$, $r = s = 0.8$ *for all panels.*

starting from a constant history of $X(s) = -0.5$ (the autonomous stable equilibrium) for $s \in [2000 + 10\tau, 2000]$ kyr BP (recall that the time unit for τ was 10 kyr) and shows only the small-amplitude response. The purple time profile is computed starting from a constant history of $X(s) = +0.5$ for $s \in [2000 + 10\tau, 2000]$ kyr BP and shows the large-amplitude response. As both responses are perturbations of attractors, they will not change when we perturb the initial conditions slightly (apart from a short transient) [32]. This persistence breaks down as one increases the forcing amplitude u. Numerical experiments by Quinn et al. [32] discovered that this breakdown leads to a noticeable transition between these two responses. Figure 3(b) summarizes the transition for forcing amplitudes $u \in [0, 0.25]$ and fixed delay $\tau_{\mathrm{bist}} = 1.45$ in the bistable region r_{el} of Figure 2:

- The transition occurs prominently with respect to change of forcing strength u near $u \approx 0.08$.
- It occurs with respect to time, consistently between 700 and 750 kyr BP. This agrees with the timing of the MPT according to palaeorecords (see upper panel of Figure 1).
- Not visible in Figure 3(b), but discussed in [32], the transition occurs independent of small perturbations to the initial condition.

The blue time profile in Figure 3(c) is one example of a solution that displays the transition in time (at $u = 0.15$). It shows a small-amplitude response up until about 750 kyr BP, when it then transitions to the large-amplitude response. For comparison Figure 3(c) also shows the red time profile, which is the response for identical u, but for delay $\tau_{\mathrm{ref}} = 1.25$ outside of the bistable region, where only the small-amplitude response exists. The color coding in the overview Figure 3(b) is defined by the distance between the responses at $\tau = \tau_{\mathrm{bist}} = 1.45$ and reference trajectories $\tau = \tau_{\mathrm{ref}} = 1.25$ with identical forcing strength $u \in [0, 0.25]$ and identical initial histories (at $X(s) = -0.5$). So, for example, at $u = 0.15$ the color in Figure 3(b) is defined by the distance between the blue and red profiles in Figure 3(c).

The supplementary material includes a video (M120307_01.mp4 [local/web 940KB]) of trajectories for $\tau = 1.45$ (in blue) and $\tau = 1.25$ (reference, red) as they change with increasing

u, where more examples of MPT-like transitions can be seen. The fact that the system favors this time period to transition is beyond the scope of this paper, but we will describe a possible mechanism for a simplified forcing scenario in section 4.

In this study we will focus on the first feature of the transition: the transition with respect to forcing strength u. As we will show, the transition in forcing amplitude u occurs already when the model is subject to periodic forcing. Studying the periodic case first will help us predict the range of forcing amplitudes that allows a temporal transition similar to the MPT (possibly timed by a distinct property of the astronomical forcing around the transition). Since 41 kyr is the prominent periodicity in the astronomical forcing, we expect that the system shows a similar transition to a large-amplitude response when varying the forcing amplitude u of a periodic forcing with period 41 kyr.

3. Periodic forcing.

We are interested in the behavior of this model when a sinusoidal forcing with period 41 kyr is included. This corresponds to the most prominent frequency found in orbital forcing—the obliquity variations, i.e., the changes in the angle between the rotational and orbital axes. Thus, we choose

$$F_P(t) = \sin(2\pi t/T). \tag{3}$$

The forcing period is $T = 4.1$, corresponding to 41 kyr.

This forcing is included in the same way as the astronomical forcing F_I,

$$\dot{X}(t) = -pX(t-\tau) + rX(t) - sX(t-\tau)^2 - X(t-\tau)^2X(t) - uF_P(t). \tag{4}$$

DDE (4) is a dynamical system with the phase space $U = C([-\tau, 0]; \mathbb{R})$, where $C([-\tau, 0]; \mathbb{R})$ is the space of continuous functions on the interval $[-\tau, 0]$ with the maximum norm $\|X\|_0 = \max\{|X(t)| : t \in [-\tau, 0]\}$. At any given time $t \geq 0$, the state is $X_t : [-\tau, 0] \ni s \mapsto X(t+s) \in \mathbb{R}$. For sufficiently small values of u and $\tau \in r_{\text{el}}$, there exist

- a stable small-amplitude periodic orbit (with period T), which is a perturbation of the stable equilibrium at $u = 0$; and
- a stable quasiperiodic large-amplitude solution, which is a perturbation from the large-amplitude periodic orbit at $u = 0$.

These two attractors will persist for a range of u, and we will refer to them as the *small-amplitude response* and the *large-amplitude response*, as we did in the case of astronomical forcing. Both types of stable long-time regimes are shown in Figure 4(a), including a transient. We observed in simulations that the large-amplitude response changes from quasiperiodic to chaotic as u increases. Large-amplitude chaotic responses have been observed previously in conceptual ice age models subject to periodic forcing in the literature. Ashwin, Camp, and von der Heydt [2] find significant regions of chaotic responses for the van der Pol–Duffing oscillator, the Saltzman and Maasch 1991 model [35], and the Paillard and Parrenin 2004 model [31]. The chaos exists both for simple periodic forcing defined by (3) and more complex quasiperiodic forcings. In contrast to our scenario, in [2] all of the models were considered in parameter regions where the unforced dynamics has a single large-amplitude stable periodic orbit. Our simulations suggest that large-amplitude chaotic solutions are also present in a periodically forced bistable regime.

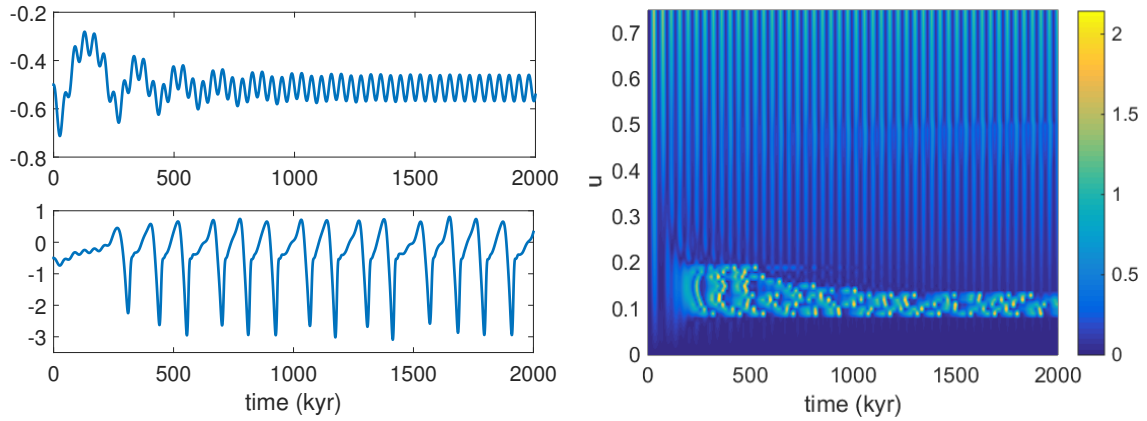

(a) Top: $u = 0.08$, Bottom: $u = 0.09$ (b) Distance from unforced stable equilibrium

Figure 4. (a) *Example trajectories of* (4) *for two qualitatively different long-time regimes. Top: small-amplitude response (a small-amplitude periodic orbit). Bottom: large-amplitude response (longer time series suggest that it is chaotic).* (b) *Distance of solution* X *from* $X_0 : t \mapsto -0.5$ *(a stable equilibrium of the unforced system) for varying forcing amplitudes* u*. Other parameters:* $\tau = 1.55$, $T = 4.1$, $p = 0.95$, $r = s = 0.8$, $\phi = 0$*; initial history,* $X_0(s) = -0.5$ *for* $s \in [-\tau, 0]$.

The heat map in Figure 4(b) shows the model response over a larger range of forcing amplitudes u. For Figure 4(b) we keep the delay constant at $\tau = 1.55$ and increase u from 0 to 0.75. All trajectories start from the constant initial history $X_0 : [-\tau, 0] \ni s \mapsto -0.5 \in \mathbb{R}$ corresponding to the stable equilibrium of the unforced system. We then compute the distance of $X_t : [-\tau, 0] \ni s \mapsto X(t+s) \in \mathbb{R}$ to X_0, using the mean absolute error (MAE), $\mathrm{MAE}(X_t, X_0) = \frac{1}{\tau}\int_{-\tau}^{0} |X_t(s) - X_0(s)| ds$. Bright colors in Figure 4(b) indicate large distances, corresponding to large-amplitude responses. We notice an obvious shift in behavior between $u = 0.08$ and $u = 0.09$, where the model goes from exhibiting the small-amplitude periodic orbit to following the large-amplitude solution. This lower threshold is similar to the observations when applying nonperiodic insolation forcing (compare to Figure 3(b)).

3.1. Bifurcation analysis. In order to examine the cause of the shift in behavior observed in Figure 4(b), we first consider a numerical bifurcation analysis of DDE (4). The forcing period is kept constant at $T = 4.1$ (corresponding to 41 kyr). We consider forcing amplitudes $u \in [0, 0.75]$ and delays τ in the bistable region $\tau \in r_{\mathrm{el}} \approx [1.295, 1.625]$ of the unforced system ($u = 0$).

Figure 5(a) shows the bifurcations of the small-amplitude periodic orbit. Bifurcations only occur for $\tau > 1.53$ and $u > 0.38$. For a range of $u > 0.4$ there exists a cascade of period doubling bifurcations for increasing τ, evidence of which is also visible in Figure 4(b). Figure 5(b) shows a cross-section of the two-parameter bifurcation diagram Figure 5(a) along the horizontal line $u = 0.55$ displaying the maximum and minimum of the periodic orbits on the y-axis. We observe that the small-amplitude motion does *not* experience any bifurcation for $u < 0.3$. Moreover, because the bifurcations are restricted to large values of τ, they cannot be used to explain the transition in time observed in Figure 3(b), which is present for all τ throughout the bistable region; see [32]. Therefore periodic forcing, even with a slowly

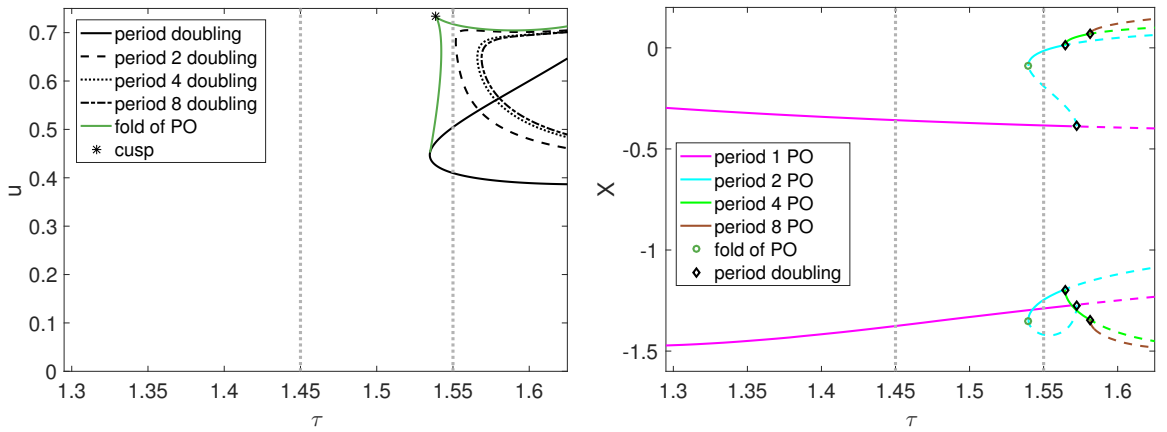

(a) Bifurcation diagram for varying τ and u (b) Cross-section for $u = 0.55$

Figure 5. *Bifurcations of small-amplitude periodic orbit. Dotted vertical lines indicate values of τ used in subsections 3.2 to 3.4; other parameters: $T = 4.1$, $\tau = 1.55$, $p = 0.95$, $r = s = 0.8$.*

time-dependent modulated amplitude, is not sufficient to induce the MPT-like transition.

The large amplitude solution also goes through some bifurcations. We do not show a detailed bifurcation analysis, but evidence of the collapse of the large-amplitude solution can be seen in Figure 4(b). These large responses are stable in a range of forcing amplitudes $u \in [0.09, 0.15]$ in Figure 4(b). For $u \in [0.15, 0.2]$ the trajectories make transient large-amplitude excursions before converging to a small-amplitude periodic orbit, which suggests a collapse of the (then chaotic) large-amplitude attractor.

As Figure 5(a) establishes, the observed transition in Figure 4(b) from small- to large-amplitude oscillations at $u = 0.09$ must have been caused by some phenomenon other than a bifurcation. Since the unforced system is bistable for $\tau \in r_{\text{el}}$, we expect this bistability to persist for small forcing amplitudes u. Thus, the initial history may cross from the basin of attraction of the small-amplitude periodic orbit to the basin of attraction of the large-amplitude response. Both example trajectories in Figure 4(a) started from the same initial history but were computed with slightly different forcing amplitude ($u = 0.08$ and $u = 0.09$). Figure 4(b) suggests that the constant initial history $X_0 : s \mapsto -0.5$ leaves the basin of attraction of the small-amplitude periodic orbit at the lower threshold $u \approx 0.09$.

3.2. Dynamics on a two-dimensional slow manifold. Since DDEs are infinite-dimensional, it is not feasible to determine the basin of attraction in all dimensions. However, previous studies have proven results of Poincaré–Bendixson type (there exists a plane in $\mathbb{R}^2$ such that trajectories cannot cross each other) for scalar DDEs with monotone feedback [27, 26]. These are DDEs of the form

$$\dot{x}(t) = f(x(t), x(t-\tau)), \text{ where } f(0,0) = 0 \text{ and } \delta y\, f(0,y) > 0 \text{ for all } y \neq 0,\ \delta \in \{-1, 1\}, \tag{5}$$

($\delta = 1$ corresponds to positive delayed feedback, $\delta = -1$ corresponds to negative delayed feedback). The right-hand side $f(X(t), X(t-\tau))$ in (1) does not satisfy the feedback conditions in (5) since, for our right-hand side f, $f(0,y) = -py - sy^2$ changes sign also at

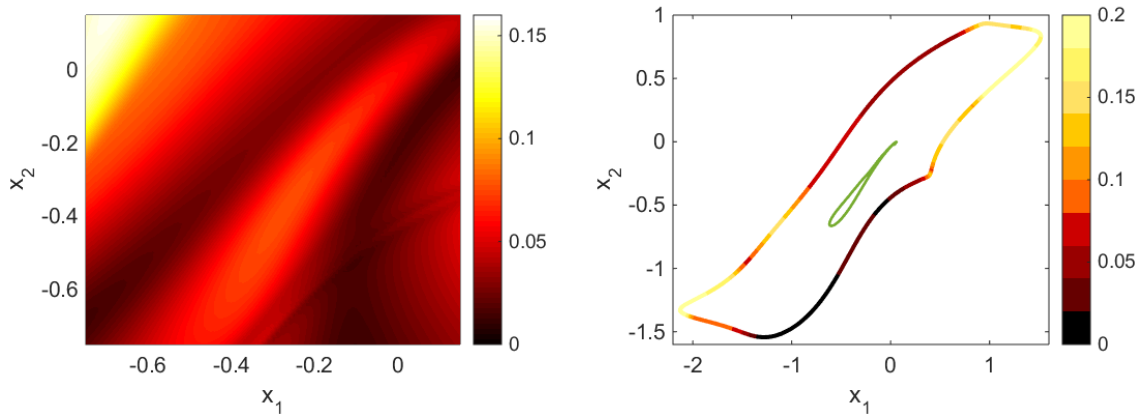

Figure 6. *Spectral gap of linearization of* M^1 (a) *on the domain* $L([-0.75, 0.15] \times [-0.75, 0.15])$ *and* (b) *on the boundary for which the Jacobian of* RM^1L *becomes singular. Color indicates the ratio between the third and second largest singular values of* ∂M^1. *The green boundary in figure* (b) *depicts the basin discussed in subsections* 3.3 *and* 3.4. *Parameters:* $u = 0.09$, $T = 4.1$, $\tau = 1.55$, $p = 0.95$, $r = s = 0.8$, $\phi = 0$.

$y = -p/s = -1.1875$, which is reached in the unforced large-amplitude periodic orbit (see Figure 2). However, the phase portrait in Figure 2 suggests that the unforced DDE (4) (with $u = 0$) has an attracting two-dimensional slow manifold. We expect this manifold to persist for small forcing amplitudes u.

The apparent existence of an attracting two-dimensional slow manifold suggests that it may be possible to use an implicit computational dimension reduction introduced by Kevrekidis et al. as *equation-free methods* (see reviews [21, 22]). The method can be used under the assumption that a high-dimensional system has a low-dimensional attracting slow manifold. The framework was originally developed for analysis of emergent macroscopic dynamics in stochastic or chaotic multiparticle simulations. Primarily, demonstrations of its use have focused on analysis of equilibria or relative equilibria, e.g., bifurcation analysis (see [39] for a recent general implementation) or control design [38]. In our case the high-dimensional system is the DDE (4) (discretized by N history points in practice) and the slow manifold is two-dimensional. Thus, the underlying problem is simpler than multiparticle systems as it has a well-understood time-scale separation (demonstrated in Figure 6(a)). However, we will construct the slow stable manifold of the period-one saddle periodic orbit, which is a more complex object than typically investigated with equation-free methods. The stable manifold will then pinpoint precisely the boundary of the basin of attraction inside the slow manifold.

The general idea of the equation-free framework is as follows. One defines a *lifting* function L from the low-dimensional space $\mathbb{R}^2$ to the infinite-dimensional space of the DDE (e.g., $U = C([-\tau, 0]; \mathbb{R})$). One then evolves the dynamics on the infinite-dimensional space using a simulator of the high-dimensional system (the *evolution* map M). Here, this corresponds to solving DDE (4) up to a time t and extracting solution $X(s)$ for $s \in [t-\tau, t]$. Finally, one defines a *restriction* function R to project the infinite-dimensional solution $X_t \in U = C([-\tau, 0]; \mathbb{R})$ back into the low-dimensional space. In our case RX_t is $(X_t(0), X_t(-\tau)) = (X(t), X(t-\tau)) \in$

$\mathbb{R}^2$. In summary, in our particular case, we have

$$L : \mathbb{R}^2 \ni (x_1, x_2) \mapsto (X_0, \tilde{X}_0) \in \mathbb{R} \times \mathbb{L}^\infty([-\tau, 0]; \mathbb{R}) =: U^{\odot,*}, \tag{6}$$
lifting
where $X_0 = x_1$ and $\tilde{X}_0(s) = x_2$ for $s \in [-\tau, 0]$,

$$M_{t,t_0} : U^{\odot,*} \ni (y_0, \tilde{y}) = X_{t_0} \mapsto X_{t_0+t} \in U \quad \text{for } t \geq \tau, \tag{7}$$
evolution map

$$R : U \ni X \mapsto (X(0), X(-\tau))^T \in \mathbb{R}^2. \tag{8}$$
restriction

The range of L, called $U^{\odot,*}$, admits discontinuous bounded segments and is a natural extension of the phase space $U = C([-\tau, 0]; \mathbb{R})$ of the DDE (4). Trajectories starting from $U^{\odot,*}$ return to the smaller phase space U after time τ. See Appendix A for further comments.

The equation-free approach is then based on the two-dimensional map

$$RM_{t,0}L : \mathbb{R}^2 \ni (x_1, x_2)^T \mapsto (X(t), X(t-\tau))^T \in \mathbb{R}^2. \tag{9}$$

The definition of the map in (9) means that for a given pair $(x_1, x_2) \in \mathbb{R}^2$, we define the initial history of (4) as $X(0) = x_1$ and $X(s) = x_2$ for $s \in [-\tau, 0)$, simulate the DDE up to time $t \geq \tau$ from this history, and then use $(X(t), X(t-\tau))^T$ as the result of the map. From this point onward we will refer to (x_1, x_2) as the argument of the map defined in (9).

In our computations we approximate elements $(X_0, \tilde{X}_0) \in U^{\odot,*}$ by vectors $Y \in \mathbb{R}^N$, where Y_k is an approximation of $\tilde{X}_0(-\tau(N-k)/(N-1))$ for $1 \leq k < N$ and $Y_N = X_0$. We use the discretized map M based on the Euler–Heun integration approximation with $h = 0.01$, where a single step has the form

$$\begin{aligned} &M_{h,t} : \mathbb{R}^N \ni Y \mapsto (Y_2, \ldots, Y_N, Y_N + h(f_0 + f_E)/2)^T \in \mathbb{R}^N, && \text{where} \\ &f_0 = f(t, Y_N, Y_1, u), \quad Y_N^0 = Y_N + hf_0, \quad f_E = f(t+h, Y_N^0, Y_2, u), && \text{and} \\ &\quad f(t, x_1, x_2, u) = -px_2 + rx_1 - sx_2^2 - x_2^2 x_1 - uF_P(t) \end{aligned}$$

is the right-hand side of the DDE (4). For larger time spans we apply the composition rule $M_{t+s,r} = M_{t,s+r} \circ M_{s,r}$ for $s, t \geq 0$, such that the discretization using $N - 1 = s/h$ steps converges to the continuous map $M_{t+s,s}$ uniformly for bounded $t \geq \tau$ and bounded initial values in $U^{\odot,*}$. We restrict ourselves to stroboscopic maps $M_{t+s,s}$, where t is a multiple of the period: $t = kT$ with $k \in \mathbb{Z}$ and $T = 4.1$, such that we may write

$$M^k Y = M_{kT,0}(Y)$$

for integers $k \geq 0$. The map $M^k : \operatorname{rg} L \to \operatorname{dom} R$ ($\operatorname{rg} L$ is the range of L, $\operatorname{dom} R$ is the domain of definition of R) is autonomous and smooth, since $M_{(k+j)T,jT} = M_{kT,0}$ for all integers $k \geq 0$ and j, and periodic forcing with period T. With this notation, M^{k+j} equals $M^k M^j$. Compatible with the discretization of M, the discretizations of lifting and restriction are

$$\begin{aligned} &L : \mathbb{R}^2 \ni (x_1, x_2)^T \mapsto (x_2, \ldots, x_2, x_1)^T \in \mathbb{R}^N, \\ &R : \mathbb{R}^N \ni Y \mapsto (Y_N, Y_1)^T \in \mathbb{R}^2. \end{aligned}$$

Before proceeding with the application of the equation-free methods, we give numerical evidence that a two-dimensional slow invariant manifold is indeed present. Figure 6(a)

shows that the linearization of the map M^1 has a spectral gap after the first two eigenvalues such that ∂M^1 is a small perturbation of a rank 2 matrix for all y in a neighborhood of $L([-0.75, 0.15] \times [-0.75, 0.15])$. This is numerical evidence for the suspected time-scale separation leading to a two-dimensional slow manifold. We do not need to construct the slow manifold explicitly, but rather may construct an approximate two-dimensional map $\mathcal{M}_\ell$ from the slow manifold back to itself implicitly, using coordinates in $\mathbb{R}^2$:

$$\mathcal{M}_\ell : \mathbb{R}^2 \ni x \mapsto y \in \mathbb{R}^2, \quad \text{where } y \text{ is the solution of} \quad RM^{\ell+1}Lx = RM^{\ell}Ly. \tag{10}$$

The integer ℓ is the *healing time* in the notation of [21, 22]. The map $\mathcal{M}_\ell$ approximates the true stroboscopic map generated by the DDE (4) on the slow manifold [37]. An intuitive explanation of why the implicitly defined map M_ℓ is a valid approximation of the stroboscopic map on the slow manifold is given, for example, in [28, 37]: the map L maps $\mathbb{R}^2$ to a subspace that is assumed to be inside the basin of attraction of the attracting slow manifold. Thus, for both sides of the implicit definition (10) the map $M^\ell L$ maps the element of $\mathbb{R}^2$ into the slow manifold (rather, very close to it, if ℓ is large enough). This map $M^\ell L$ is a diffeomorphism (a chart) between the slow manifold and $\mathbb{R}^2$. Calling $u_x = M^\ell Lx$ and $u_y = M^\ell Ly$, which are both objects inside the slow manifold in the high-dimensional space, the implicit definition (10) requires $RMu_x = Ru_y$. If R is a diffeomorphism between the slow manifold and $\mathbb{R}^2$ (a genericity condition), then this requirement implies that $Mu_x = u_y$. Thus, M_ℓ, given by (10), approximates the map M on the slow manifold in the coordinates given by the chart $M^\ell L$.

The approximation (10) improves for increasing healing time ℓ if lifting L and restriction R satisfy some genericity conditions (implying that the map R is a diffeomorphism between the slow manifold and $\mathbb{R}^2$, and that $RM^\ell L : \mathbb{R}^2 \to \mathbb{R}^2$ is a diffeomorphism). The convergence result in [37] does not require a large separation of time scale, only a sufficiently large healing time. In our case, $\ell = 1$ (a healing time of one period $T = 4.1$) is sufficient; the results only change by less than 10^{-2} when increasing ℓ to 2 (a large ℓ increases the condition number of $\partial[RM^\ell L]$).

Within this persistent slow manifold the time-T map of the forced DDE (4) is a locally invertible two-dimensional map. For two-dimensional maps the basin of attraction for a periodic orbit is often bounded by the stable manifold of a saddle periodic orbit. Figure 6(a) justifies using a planar rectangle in $\operatorname{dom} L$ to visualize the basins of attraction in the slow manifold. Furthermore, since we can evaluate the stroboscopic map on the two-dimensional slow manifold by using $\mathcal{M}_\ell$, we can employ algorithms designed for the computation of stable manifolds of fixed points in planar maps. In particular, we continue all three fixed points present for zero forcing ($u = 0$; see Figure 2) in the parameter u, using the defining equation

$$RM^\ell Lx_{\text{fix}} = RM^{\ell+1}Lx_{\text{fix}},$$

which is a system of two equations for the two-dimensional variable x_{fix} and the parameter u (results will be shown for healing time $\ell = 1$). One of the fixed points is of saddle type. The equation-free construction of a map from the slow manifold back to itself via (10) permits us to extend specialized algorithms for planar maps such as the algorithm for the computation of the stable manifold of a saddle fixed point for maps that are not globally invertible, proposed by England, Krauskopf, and Osinga [12] and originally implemented for two-dimensional maps

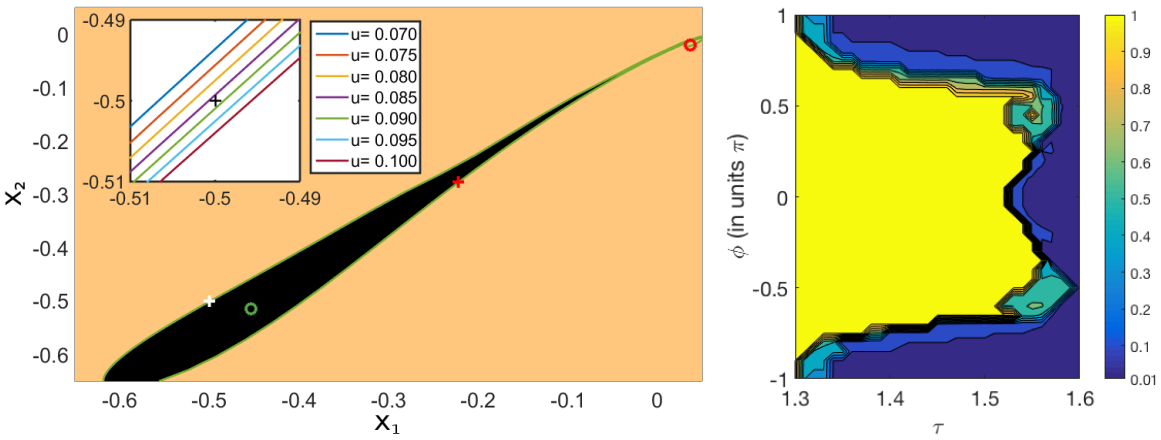

(a) $\tau = 1.55$ (b)

Figure 7. (a) *Basin of attraction for the stable small-amplitude periodic orbit for* $\tau = 1.55$. *Initial conditions in the black regions are attracted to the stable small-amplitude periodic orbit (green circle) intersected with* $\operatorname{dom} L$. *The white cross indicates the initial condition* $(x_1, x_2) = (-0.5, -0.5)$ *used to create Figure 4(b). The red circle is the unstable small-amplitude periodic orbit, while the red cross represents the saddle periodic orbit. Figure zoom-in (top left) shows stable manifold for different values of* u *close to the initial condition* $(x_1, x_2) = (-0.5, -0.5)$ *(black cross). The basin was computed using simulations of (4) with initial history* $X(0) = x_1$ *and* $X(s) = x_2$ *for* $s \in [-\tau, 0)$. *The basin boundaries (colored lines) were computed using the method described in Appendix B.* (b) *Threshold values for* u *at which a transition to the large-amplitude response is observed as a function of delay* τ *and phase shift* ϕ *with initial history* $X(s) = -0.5$ *for* $s \in [-\tau, 0]$. *Values for which no transitions were observed are shown with* $u = 1$. *Other parameters for both figures:* $T = 4.1$, $p = 0.95$, $r = s = 0.8$.

in `DsTool`. Since the map $\mathcal{M}_\ell$ is implicitly defined, the algorithm as originally implemented would require the solution of the nonlinear system (10) every time the map gets evaluated. This turns out to be unnecessary: we modify the stable manifold algorithm such that it does not require any solution of a nonlinear system (see Appendix B for a brief explanation). The stable manifold of the saddle fixed point will determine the basin of attraction for the stable fixed point (the other fixed point is a source for all u) on the slow manifold.

The large-amplitude response (attracting initial conditions on the other side of the stable manifold) is partially outside of the domain of validity of the coordinates introduced by lifting L and restriction R. Figure 6(b) shows the curve in the $\operatorname{dom} L$ plane along which the Jacobian of RM^1L becomes singular, which violates one of the assumptions made in the implicit definition (10) of $\mathcal{M}_1$. Outside of this curve (where the large-amplitude solution lies), our chosen plane is no longer valid. However, the spectral gap values indicate that the dynamics may still be confined to a two-dimensional slow manifold.

3.3. Basins of attraction and stable manifold in the plane.

Figure 7(a) shows the basins in the rectangle $[-0.65, 0.05] \times [-0.65, 0.05]$ for $u = 0.09$.

The initial condition $x_1 = x_2 = -0.5$, corresponding to a constant initial history $X(s) = -0.5$ for $s \in [-\tau, 0]$, was used in the parameter scan for increasing forcing amplitude u, depicted in Figure 4(b). This point is indicated by a white cross in Figure 7(a). Black regions

in Figure 7(a) are initial histories $X(0) = x_1$ and $X(s) = x_2$ for $s \in [-\tau, 0)$ that converge to the stable small-amplitude periodic orbit in the center of the black region. The beige region contains initial histories that escape to the large-amplitude response. The saddle fixed point is located near $(-0.2, -0.3)$. Its stable manifold (in green) is the boundary between the two basins of attraction. The inset in Figure 7(a) shows how the stable manifold of the saddle fixed point changes as the forcing amplitude u increases. In particular, we observe how the initial condition $(-0.5, -0.5)^T$ is crossed by the stable manifold, which shifts downward as u increases. An animation of the moving basin of attraction with increasing u can be found in the supplementary material (M120307_02.mp4 [local/web 57.8KB]).

3.4. Dependence on forcing phase. As the basin of attraction in Figure 7(a) shows, the critical forcing amplitude $u = 0.09$ for the transition depends strongly on the initial condition, which we chose as $X_0 = -0.5$ (= const) for the heat map in Figure 4(b). This dependence is specific to periodic forcing, since the transition for astronomical forcing shown in Figure 3(b) is not susceptible to small perturbations of the initial conditions (as pointed out in subsection 2.2). Specifically, Quinn et al. [32] reported negative finite-time Lyapunov exponents for times before 1000 kyr BP such that a neighborhood of initial conditions leads to trajectories identical to those in Figure 3, starting from $X_0 = -0.5$, after transients. As the periodically forced DDE possesses a slow manifold (see Figure 6(a) for evidence), each initial condition in the infinite-dimensional phase space of the DDE leads to a trajectory that converges rapidly to a trajectory in the two-dimensional slow manifold. Thus, the initial condition for the periodically forced DDE should be in the plane shown in Figure 7(a) near $X_1 = X_2 = -0.5$ (since the astronomic forcing attracts us to this point and the slow manifold is attracting). Therefore the only open question is the phase of the periodic forcing. We adjust the forcing equation accordingly,

$$F_P(t) = \sin((2\pi/T)\, t - \phi), \quad \phi \in [-\pi, \pi]. \tag{11}$$

The variable ϕ represents the phase shift of the forcing. Note that the bifurcation diagram Figure 5(a) is independent of the forcing phase ϕ. However, Figure 7(b) shows that the phase affects the threshold value for the forcing amplitude u at which a transition to the large-amplitude response occurs with initial history $X(s) = -0.5$ for $s \in [-\tau, 0]$. Figure 7(b) shows contours of the smallest value of u for which we observe a transition to large-amplitude response in simulations for different forcing phases ϕ and delays τ in the bistable region r_{el} of Figure 2. For all points in Figure 7(b) we chose the initial history $X(s) = -0.5$ for $s \in [-\tau, 0]$; however, we note that changing the phase of the forcing is equivalent to considering different initial histories along a closed curve in the plane of Figure 7(a) through $(x_1, x_2) = (-0.5, -0.5)$. For some parameter combinations the response is always small amplitude. In these points we set the contour level to its maximum ($u = 1$). A distinct boundary can be seen between parameter combinations that exhibit transitions at low values of u and those that do not. For a forcing phase $\phi = \pi$, a transition can always occur within the bistable region.

In the supplementary material (M120307_03.mp4 [local/web 108KB]) we show the effect of a phase shift on the basin of attraction for the small-amplitude periodic orbit in the plane $\operatorname{dom} L$. This change of basin of attraction implies that, for some phases ϕ, trajectories from the initial history $X(s) = -0.5$ for $s \in [-\tau, 0]$ will converge to the small-amplitude periodic

orbit, while for other phases trajectories with the same initial history will converge to the large-amplitude response.

4. Conclusions. We have presented a study of a scalar DDE model for the Pleistocene when subjected to periodic forcing. The forcing period is 41 kyr, corresponding to the most prominent frequency seen in astronomical insolation variations. With this particular forcing, two stable solutions are observed at small forcing amplitudes: a small-amplitude periodic orbit and a large-amplitude, long-period response. Both responses are a perturbation to the stable solutions of the autonomous system. When the forcing amplitude is varied, we observe a threshold between convergence to the periodic orbit and convergence to the large-amplitude response. A similar threshold is also seen with astronomic forcing presented in [32], where above a critical value of forcing strength u, transitions to a large-amplitude response occur. Numerical bifurcation analysis of the small-amplitude periodic orbit shows that this threshold is outside of the region where any bifurcations occur, therefore leading us to conclude that changes in the basin of attraction for the periodic orbit and large-amplitude response are the underlying mechanism.

In order to consider basins of attraction in the infinite-dimensional setting of DDEs, we give numerical evidence that there exists a two-dimensional slow manifold on which a stable saddle and unstable periodic orbit persist. This justifies using equation-free methods to construct a stroboscopic map on the slow manifold and track the locations of its fixed points. We then apply a modified algorithm for computation of stable manifolds of saddle fixed points in planar maps to the slow manifold of the infinite-dimensional DDE without ever computing this slow manifold (original algorithm proposed by England, Krauskopf, and Osinga [12]). Details and didactic implementation of the modified algorithm for implicitly defined maps are given in the supplementary material (M120307_04.pdf [local/web 240KB]). This stable manifold forms the intersection between slow manifold and the boundary for the basin of attraction of the stable periodic orbit. We observe that the stable manifold (and with it the basin boundary) moves for increasing forcing amplitude. It crosses our chosen initial history for an amplitude around $u = 0.09$. We also scan the dependence of the basin of attraction on the phase of the forcing, which is equivalent to a change in the initial history function inside the slow manifold. We conclude that the threshold behavior observed for the periodically forced model can be attributed to a shifting basin of attraction.

Connection to astronomic forcing—a simplified scenario. The results shown in Figure 7 provide a possible mechanism behind the observations for the astronomical forcing, recalled in subsection 2.2 and in Figure 3. In particular, the geometry shown in the inset in Figure 7(a) induces a transition similar to the one shown in Figure 3(b) for a simple stepwise amplitude modulation of the periodic forcing. If we replace the constant amplitude u of the periodic forcing with a stepwise function of time,

$$u(t) = \begin{cases} \ll 1 & \text{for } t < 750\text{kyr BP}, \\ u_{\text{end}} & \text{for } t \geq 750\text{kyr BP}, \end{cases} \tag{12}$$

then the response X will be attracted to the area near the black cross in the inset of Figure 7(a) during the time $t \in [2000, 750]$ kyr BP, independent of small perturbations of the initial condition (recall that the equilibrium for $u = 0$ is at this point $X = -0.5$). At $t = 750$ kyr

BP, after the shift in u, the state X will be outside of the basin of attraction of the fixed point for the new parameter value u_{end} (above the colored curve for u in Figure 7(a)) if u_{end} is above a critical value (≈ 0.09). Thus, X will escape toward the large-amplitude response after $u = 750$ kyr BP. Hence, for a stepwise periodic forcing with (12) one would make observations very similar to those listed in subsection 2.2, including the sudden transition with respect to time, with respect to u_{end}, and the independence from small perturbations to the initial conditions. Scenarios where the shift of a basin of attraction due to a parameter change causes a transition have been studied using the notion of *rate-induced tipping* [40, 3, 33, 1]. The scenario (12) corresponds to an infinite rate of change in the parameter (the forcing amplitude u) at time $t = 750$ kyr BP. For this scenario Ashwin, Perryman, and Wieczorek [3] developed the concept of breakdown of basin forward stability, which generalizes the scenario described above for forcing (12).

The stepwise amplitude modulation (12) is simpler than the astronomic forcing (Figure 1, bottom panel). However, Quinn et al. [32] showed for astronomic forcing that finite-time Lyapunov exponents along the trajectories in Figure 3(b) remain negative for $u < 0.22$ prior to transition time (~ 750 kyr BP). This implies that all trajectories from an open neighborhood of the unforced stable equilibrium are attracted to the same small-amplitude response prior to transition time. Therefore the shift of basins of attraction is likely to be involved in the mechanism behind the observations in Figure 3 and of Quinn et al. [32].

The numerical bifurcation analysis of the small-amplitude periodic orbit in Figure 5 also illustrates that no bifurcation occurs for $\tau < 1.53$. This implies that even a gradual drift in the forcing amplitude (e.g., a slow time-dependent forcing amplitude $u(t)$ of the periodic forcing) is not enough to cause the temporal transition observed with the quasiperiodic forcing in Figure 3(b). This supports the conclusions of [32] that the phenomenon observed in Figure 3(b) is not related to a slow passage through a classical bifurcation, including bifurcations of periodic orbits. This is different from the idea presented in [11], where in simple oscillator models under periodic forcing a generic transcritical bifurcation is necessary for the system to transition between the smaller-amplitude 41 kyr cycle to the large-amplitude 100 kyr response. We therefore conjecture that the transition is an effect of the near-quasiperiodic modulation of the basic periodic forcing studied in this paper, which is present in the astronomical forcing, resulting in a more complicated version of the rate-induced tipping phenomenon obtained for the stepwise amplitude modulation (12). This may require application of the general quasiperiodic theory of Fuhrmann, Gröger, and Jäger [14] or the pullback attractor framework outlined in Chekroun, Ghil, and Neelin [7].

Appendix A. Extension of the phase space $U = C([-\tau, 0]; \mathbb{R})$. This appendix gives a brief explanation for the extension of the phase space of DDEs, from which we permit initial conditions of the stroboscopic map M in subsections 3.2 to 3.4. The space $\mathbb{R} \times \mathbb{L}^\infty([-\tau, 0]; \mathbb{R})$ (called $U^{\odot,*}$ in the terminology of [9]) is a natural extension of the phase space $U = C([-\tau, 0]; \mathbb{R})$ of the DDE (4). The trajectories of the DDE (4) starting from initial values in $U^{\odot,*}$ admit discontinuous essentially bounded initial history segments $\tilde{X}_0 : [-\tau, 0] \mapsto \mathbb{R}$ and have X_0 as the right-side limit for $t \searrow 0$. For an element $(X_0, \tilde{X}_0)$ of $U^{\odot,*}$, X_0 is usually called the *head point*, while $\tilde{X}_0$ is the *history segment*. The notation $\mathbb{L}^\infty([-\tau, 0]; \mathbb{R})$ refers to the space of essentially bounded functions on $[-\tau, 0]$ with essential maximum norm

$\|\tilde{X}_0\|_0 = \inf\left\{m \geq 0 : \mathrm{Leb}\{t \in [-\tau, 0] : |\tilde{X}_0(t)| \geq m\} = 0\right\}$ ($\mathrm{Leb}\, A$ is the Lebesgue measure of a set $A \subset \mathbb{R}$). The special role of the head point X_0 (compared to the remainder of the history segment $\tilde{X}_0$) becomes clear when restating a DDE using the equivalent variation-of-constants identity. In our special case of a DDE of the form $\dot{X}(t) = f(X(t), X(t-\tau), t)$ with fixed discrete delay τ this identity simplifies for $t \in [0, \tau]$ to

$$X(t) = X_0 + \int_0^t f(s, X(s), \tilde{X}_0(s-\tau))\mathrm{d}\, s.$$

This identity makes clear that, for example, changing $\tilde{X}_0$ on a set of Lebesgue measure 0 does not have any effect on the solution $X(t)$ for $t > 0$, while changing X_0 does.

As explained in the textbook [9] trajectories starting from an element in the larger space $U^{\odot,*}$ return to the smaller phase space U after time τ and the dependence $U^{\odot,*} \ni (X_0, \tilde{X}_0) \mapsto X_t \in U$ of the solution on its initial history is as regular as the right-hand side of the DDE (4). Thus,

$$U^{\odot,*} \ni X \mapsto M(t, t_0; X) \in U$$

is smooth for all $t \geq \tau$ and $t_0 \in \mathbb{R}$.

Appendix B. Summary of modification of stable manifold algorithm by England, Krauskopf, and Osinga [12]. The supplementary material (M120307_04.pdf [local/web 240KB]) describes how one can modify the search circle (SC) algorithm for stable manifolds in [12] for maps $\mathcal{M}_\ell$ given implicitly through

$$\mathcal{M}_\ell : \mathrm{dom}\, L \ni x \mapsto y \in \mathrm{dom}\, L, \quad \text{where } y \text{ is the solution of } \quad RM^{\ell+1}Lx = RM^{\ell}Ly. \tag{13}$$

The supplement (M120307_05.zip [local/web 920KB]) also contains a didactic implementation in MATLAB (`Gnu Octave` compatible) of the algorithm, a demonstration script reproducing the manifold in Figure 7(a), and scripts reproducing some benchmark test examples from [12] (for the shear map, the modified Ikeda map, and the primary stable curve of the modified Gumowski map; see [12] for a review of the properties and history of these examples).

The original SC algorithm [12] grows the stable curve of a map $\mathcal{M}_\ell$ iteratively, approximating the stable curve by a (linear) interpolation of a sequence of k points $S^k = (x^0, \ldots, x^k)$ in $\mathbb{R}^2$. At step $k+1$ a point x^{k+1} is added. The new point x^{k+1} lies on a search circle arc with a small adaptively chosen radius Δ around x^k. The point x^{k+1} is defined by the requirement that it is an intersection of the image of this search circle under $\mathcal{M}_\ell$ with the previously computed curve S^k. In particular, the algorithm [12] does not rely on root-finding using Newton iterations, but rather on a bisection to find the intersection between image of the search circle and previous manifold. In principle, this algorithm could be applied directly if one solves the defining system (13), $RM^{\ell+1}Lx = RM^{\ell}Ly$, for y every time the original algorithm applies its map (in our case $\mathcal{M}_\ell$) to a point $x \in \mathbb{R}^2$. However, a modification of the SC algorithm avoids the need to solve the nonlinear equation (13). Instead of a single sequence (and interpolating curve) S^k one maintains two curves, $S_L^k = (x_L^0, \ldots, x_L^k)$ in $\mathrm{dom}\, L$ and $S_R^k = (x_R^0, \ldots, x_R^k)$ in $\mathrm{rg}\, R$, with $x_R^j = RM^{\ell}Lx_L^j$. Then one searches for x_L^{k+1} by finding an intersection of the map $RM^{\ell+1}L$ image of the search circle of radius Δ around x_L^k in $\mathrm{dom}\, L$ with the curve S_R^k in $\mathrm{rg}\, R$ (note the power $\ell+1$ in the mapping). Once one found this point x_L^{k+1}, for which

$RM^{\ell+1}Lx_L^{k+1} \in S_R^k$, one adds x_L^{k+1} to S_L^k and $x_R^{k+1} = RM^{\ell}Lx_L^{k+1}$ (note the power ℓ of M in the mapping) to S_R^k. Otherwise, the same rules on angles and radii for acceptance of points apply as in [12].

Acknowledgments. We would like to thank the following people for their valuable discussions and input: Timothy Lenton, Peter Ashwin, Peter Ditlevsen, Martin Rasmussen, Tobias Jäger, Flavia Remo, Hassan Alkhayuon, Paul Ritchie, and Damian Smug. Additionally, we would like to thank the CRITICS, PEN, and ReCoVER networks for enabling this collaboration.

REFERENCES

[1] H. M. Alkhayuon and P. Ashwin, *Rate-induced tipping from periodic attractors: Partial tipping and connecting orbits*, Chaos, 28 (2018), 033608.
[2] P. Ashwin, C. D. Camp, and A. S. von der Heydt, *Chaotic and non-chaotic response to quasiperiodic forcing: Limits to predictability of ice ages paced by Milankovitch forcing*, Dyn. Stat. Clim. Syst., 3 (2018), dzy002.
[3] P. Ashwin, C. Perryman, and S. Wieczorek, *Parameter shifts for nonautonomous systems in low dimension: Bifurcation- and rate-induced tipping*, Nonlinearity, 30 (2017), pp. 2185–2210.
[4] A. L. Berger, *Long-term variations of daily insolation and quaternary climatic changes*, J. Atmospher. Sci., 35 (1978), pp. 2362–2367.
[5] K. Bhattacharya, M. Ghil, and I. Vulis, *Internal variability of an energy-balance model with delayed albedo effects*, J. Atmospher. Sci., 39 (1982), pp. 1747–1773.
[6] M. I. Budyko, *The effect of solar radiation variations on the climate of the Earth*, Tellus, 21 (1969), pp. 611–619.
[7] M. D. Chekroun, M. Ghil, and J. D. Neelin, *Pullback attractor crisis in a delay differential ENSO model*, in Advances in Nonlinear Geosciences, Springer, 2018, pp. 1–33.
[8] M. Crucifix, *Oscillators and relaxation phenomena in Pleistocene climate theory*, Phil. Trans. R. Soc. A, 370 (2012), pp. 1140–1165.
[9] O. Diekmann, S. van Gils, S. Verduyn Lunel, and H.-O. Walther, *Delay Equations*, Appl. Math. Sci. 110, Springer-Verlag, 1995.
[10] H. A. Dijkstra, *Nonlinear Climate Dynamics*, Cambridge University Press, 2013.
[11] P. D. Ditlevsen and P. Ashwin, *Complex climate response to astronomical forcing: The middle-Pleistocene transition in glacial cycles and changes in frequency locking*, Frontiers Phys., 6 (2018), 62.
[12] J. P. England, B. Krauskopf, and H. M. Osinga, *Computing one-dimensional stable manifolds and stable sets of planar maps without the inverse*, SIAM J. Appl. Dyn. Syst., 3 (2004), pp. 161–190, https://doi.org/10.1137/030600131.
[13] H. Engler, H. G. Kaper, T. J. Kaper, and T. Vo, *Modeling the Dynamics of Glacial Cycles*, preprint, https://arxiv.org/abs/1705.07387, 2017.
[14] G. Fuhrmann, M. Gröger, and T. Jäger, *Non-smooth saddle-node bifurcations* II*: Dimensions of strange attractors*, Ergodic Theory Dynam. Systems, 38 (2018), pp. 2989–3011.
[15] M. Ghil, A. Mullhaupt, and P. Pestiaux, *Deep water formation and quaternary glaciations*, Climate Dynam., 2 (1987), pp. 1–10.
[16] J. D. Hays, J. Imbrie, and N. J. Shackleton, *Variations in the Earth's orbit: Pacemaker of the ice ages*, Science, 194 (1976), pp. 1121–1132.
[17] P. Huybers, *Early Pleistocene glacial cycles and the integrated summer insolation forcing*, Science, 313 (2006), pp. 508–511.
[18] P. Huybers and I. Eisenman, *Integrated Summer Insolation Calculations*, NOAA/NCDC Paleoclimatology Program data contribution, 2006-079, 2006.
[19] J. Imbrie and K. P. Imbrie, *Ice Ages: Solving the Mystery*, Harvard University Press, 1986.

[20] H. Kaper and H. Engler, *Mathematics and Climate*, SIAM, 2013, https://doi.org/10.1137/1.9781611972610.
[21] Y. Kevrekidis and G. Samaey, *Equation-free multiscale computation: Algorithms and applications*, Rev. Phys. Chem., 60 (2009), pp. 321–344.
[22] Y. Kevrekidis and G. Samaey, *Equation-free modeling*, Scholarpedia, 5 (2010), 4847.
[23] L. E. Lisiecki and M. E. Raymo, *A Pliocene-Pleistocene stack of* 57 *globally distributed benthic δ18O records*, Paleoceanography, 20 (2005).
[24] K. Maasch, *Statistical detection of the mid-Pleistocene transition*, Climate Dynam., 2 (1988), pp. 133–143.
[25] K. A. Maasch and B. Saltzman, *A low-order dynamical model of global climatic variability over the full Pleistocene*, J. Geophys. Res. Atmosph., 95 (1990), pp. 1955–1963.
[26] J. Mallet-Paret and G. R. Sell, *The Poincaré–Bendixson theorem for monotone cyclic feedback systems with delay*, J. Differential Equations, 125 (1996), pp. 441–489.
[27] J. Mallet-Paret and H. L. Smith, *The Poincaré-Bendixson theorem for monotone cyclic feedback systems*, J. Dynam. Differential Equations, 2 (1990), pp. 367–421.
[28] C. Marschler, J. Sieber, R. Berkemer, A. Kawamoto, and J. Starke, *Implicit methods for equation-free analysis: Convergence results and analysis of emergent waves in microscopic traffic models*, SIAM J. Appl. Dyn. Syst., 13 (2014), pp. 1202–1238, https://doi.org/10.1137/130913961.
[29] M. Milankovitch, *History of radiation on the Earth and its use for the problem of the ice ages*, K. Serb. Akad. Beogr, 1941.
[30] D. Paillard, *Quaternary glaciations: From observations to theories*, Quaternary Sci. Rev., 107 (2015), pp. 11–24, https://doi.org/10.1016/j.quascirev.2014.10.002.
[31] D. Paillard and F. Parrenin, *The antarctic ice sheet and the triggering of deglaciations*, Earth Planetary Sci. Lett., 227 (2004), pp. 263–271.
[32] C. Quinn, J. Sieber, A. S. von der Heydt, and T. M. Lenton, *The Mid-Pleistocene Transition induced by delayed feedback and bistability*, Dynam. Statist. Climate Syst., 3 (2018), pp. 1–17.
[33] P. Ritchie and J. Sieber, *Probability of noise- and rate-induced tipping*, Phys. Rev. E, 95 (2017), 052209.
[34] B. Saltzman and K. A. Maasch, *Carbon cycle instability as a cause of the late Pleistocene ice age oscillations: Modeling the asymmetric response*, Global Biogeochem. cycles, 2 (1988), pp. 177–185.
[35] B. Saltzman and K. A. Maasch, *A first-order global model of late Cenozoic climatic change* II. *Further analysis based on a simplification of CO_2 dynamics*, Climate Dynam., 5 (1991), pp. 201–210.
[36] W. D. Sellers, *A global climatic model based on the energy balance of the earth-atmosphere system*, J. Appl. Meteorol., 8 (1969), pp. 392–400.
[37] J. Sieber, C. Marschler, and J. Starke, *Convergence of equation-free methods in the case of finite time scale separation with application to deterministic and stochastic systems*, SIAM J. Appl. Dyn. Syst., 17 (2018), pp. 2574–2614, https://doi.org/10.1137/17M1126084.
[38] C. I. Siettos, D. Maroudas, and I. G. Kevrekidis, *Coarse bifurcation diagrams via microscopic simulators: A state-feedback control-based approach*, Internat. J. Bifur. Chaos Appl. Sci. Engrg., 14 (2004), pp. 207–220.
[39] S. A. Thomas, D. J. Lloyd, and A. C. Skeldon, *Equation-free analysis of agent-based models and systematic parameter determination*, Phys. A, 464 (2016), pp. 27–53, https://doi.org/10.1016/j.physa.2016.07.043.
[40] S. Wieczorek, P. Ashwin, C. M. Luke, and P. M. Cox, *Excitability in ramped systems: The compost-bomb instability*, Proc. R. Soc. Lond. Ser. A Math. Phys. Eng. Sci., 467 (2011), pp. 1243–1269.